Research Article

Nano Research
2024, 17(6): 5080–5086

ISSN 1998-0124 CN 11-5974/O4
https://doi.org/10.1007/s12274-024-6529-1

Hierarchical cobalt-molybdenum layered double hydroxide arrays power efficient oxygen evolution reaction

Xinyi Zhu[1,2,§], Jiahui Lyu[1,3,§], Shanshan Wang[1], Xingchuan Li[1], Xiaoyu Wei[1], Cheng Chen[1,2] (✉), Wanida Koo-amornpattana[4], Francis Verpoort[1], Jinsong Wu[1,3], and Zongkui Kou[1,2] (✉)

[1] *State Key Laboratory of Advanced Technology for Materials Synthesis and Processing, Wuhan University of Technology, Wuhan 430070, China*
[2] *Sanya Science and Education Innovation Park of Wuhan University of Technology, Sanya 572000, China*
[3] *Nanostructure Research Center, Wuhan University of Technology, Wuhan 430070, China*
[4] *Department of Chemical Engineering, Faculty of Engineering, Mahidol University, Nakhon Pathom 73170, Thailand*
[§] *Xinyi Zhu and Jiahui Lyu contributed equally to this work.*

Received: 29 December 2023 / **Revised:** 29 January 2024 / **Accepted:** 30 January 2024

ABSTRACT

Transition metal-based layered double hydroxides (LDHs) have been capable of working efficiently as catalysts in the basic oxygen evolution reaction (OER) for sustaining hydrogen production of alkaline water electrolysis. Nevertheless, exploring new LDH-based electrocatalysts featuring both remarkable activity and good stability is still in high demand, which is pivotal for comprehensive understanding and impressive improvement of the sluggish OER kinetics. Here, a series of bimetallic (Co and Mo) LDH arrays were designed and fabricated via a facile and controlled strategy by incorporating a Mo source into presynthesized Co-based metal-organic framework (MOF) arrays on carbon cloth (CC), named as ZIF-67/CC arrays. We found that tuning the Mo content resulted in gradual differences in the structural properties, surface morphology, and chemical states of the resulting catalysts, namely $CoMo_x$-LDH/CC (x representing the added weight of the Mo source). Gratifyingly, the best-performing $CoMo_{0.20}$-LDH/CC electrocatalyst demonstrates a low overpotential of only 226 mV and high stability at a current density of 10 mA·cm^{-2}, which is superior to most LDH-based OER catalysts reported previously. Furthermore, it only required 1.611 V voltage to drive the overall water splitting device at the current density of 10 mA·cm^{-2}. The present study represents a significant advancement in the development and applications of new OER catalysts.

KEYWORDS

layered double hydroxides (LDHs), metal-organic frameworks (MOFs), array catalysts, Mo modification, electrocatalytic oxygen evolution reaction (OER)

1 Introduction

Water electrolysis is a crucial energy conversion technology that enables the transformation of water into hydrogen and oxygen by using green electric energy, offering a promising approach for hydrogen energy production [1–4]. Within the entire electrolytic process, the anodic oxygen evolution reaction (OER) is notable as the rate-determining side due to its relatively sluggish four-electron transfer mechanism [5–7]. The alkaline medium with optimized surfactant adsorption on the catalyst effectively enhances OER kinetics, making it the preferred condition for water electrolysis [8]. Consequently, the quest for high-performing transition metal-based OER electrocatalysts has become a focal point in the research realm of green hydrogen production via water electrolysis [9]. Layered double hydroxides (LDHs) have been extensively studied and utilized as efficient OER catalysts or pre-catalysts [10–14], primarily due to their layered structures that provide numerous metal active sites bearing multivalent metal ions [15]. It is well-acknowledged that these metal active sites can facilitate the OER process during the electrolytic water splitting via the more competitive lattice oxygen-involving mechanism [16–22]. Moreover, the composition of LDHs can be tailored through the selection of different metal ions and anions, thereby optimizing their electrocatalytic performance to meet stringent requirements for efficiency and stability [23]. Furthermore, LDHs possess good conductivity to enable efficient electron transmission on the catalyst surface, which enhances electrocatalytic activity and decreases the power consumption of water electrolysis [24]. Additionally, the layered structures of LDHs serve as effective barriers, shielding them from external environmental conditions such as oxides or ions, thereby relieving catalyst corrosion and enhancing catalyst longevity [25].

Atomic doping into metal oxyhydroxides to form functional LDH-based catalysts has been widely demonstrated to further synchronize the activity and long-term stability in the OER because of electronic structure altering and synergistic effect among diverse intermediate conversion. Our prior study showed that enriching the surface of CoOOH with Mo during OER led to the facilitated electron flow from Mo to Co sites, thereby improving the electrostatic adsorption of OH^- ions and promoting the OER step [26]. Nevertheless, in practical OER electrolysis, challenges related to charge and mass transfer are encountered by

Address correspondence to Cheng Chen, chengchen@whut.edu.cn; Zongkui Kou, zongkuikou@whut.edu.cn

powder catalysts, leading to the requirement of a high overpotential and rendering them susceptible to stresses associated with oxygen bubble formation. To overcome these challenges, the implementation of a self-supporting, binder-free array catalyst structure is necessary. The preference for this structure is owing to the highly ordered nature of array catalysts, which allows for the meticulous arrangement and positioning of catalytic active sites, resulting in enhanced catalytic activity and reaction selectivity [27–29]. This enhancement contributes to improved catalysis of the electrolytic water splitting, decreasing the initial potential of the reaction and reducing the energy consumption of electrolytic hydrogen production [30]. Additionally, the array structures of the catalysts boost the reaction kinetics through more efficient adsorption of reactants [31, 32]. It is noteworthy that array catalysts also offer the advantage of facilitating a uniform distribution and fixation of the catalysts, thereby enlarging their contact area and improving reaction efficiency [33–35]. The above factors collectively underscore the strong desirability of developing new array-type OER catalysts featuring both excellent activity and great stability.

With the above considerations in mind, we herein intend to design and fabricate a series of bimetallic (Co and Mo) LDH arrays by integrating more active and accessible Co and Mo sites into regular array structures coated onto carbon cloth (CC) substrates, designated as $CoMo_x$-LDH/CC with x indicating the weight of the added Mo source. To achieve this, we utilized a two-step chemical deposition process to incorporate Mo into Co-based metal-organic framework (MOF) arrays, specifically ZIF-67/CC arrays. Varying the weight loading of Mo allowed us to investigate its impact on the structure, surface morphology, chemical composition of $CoMo_x$-LDH/CC. Specifically, a series of $CoMo_x$-LDHs/CC with gradually increased amounts of a Mo precursor including 0.10, 0.15, 0.20, 0.25, and 0.30 g were prepared. Subsequently, the structural, morphological characteristics, and the chemical states of the synthesized $CoMo_x$-LDHs/CC arrays were systematically investigated. Analysis revealed noticeable changes in nanosheet thickness and curling degree, along with increasing stacking with higher Mo weight loadings. These results cause alterations in the surface topography and interlayer spacing among nanosheets, affecting the abundance of catalytically active sites and oxygen bubble diffusion dynamics. Subsequent investigation of the catalytic performance of these array-type materials for the OER in 1.0 M KOH solution demonstrated that the $CoMo_{0.20}$-LDH/CC electrocatalyst exhibited overpotentials of 226, 288, and 306 mV at 10, 50, and 100 $mA{\cdot}cm^{-2}$, respectively, surpassing all other contrast samples and most reported LDH-based catalysts. This excellent electrocatalytic performance is attributed to the modification of the electrochemical active area, enhancing the accessibility of active sites for O_2 precipitation. The present work offers a straightforward and cost-effective way to develop bimetallic LDH arrays, with the optimal $CoMo_{0.20}$-LDH/CC catalyst displaying exceptional catalytic activity and stability.

2 Results and discussion

The preparation of $CoMo_x$-LDH/CC involved precipitation and ion exchange steps, and the digital images of CC, ZIF-67/CC, and $CoMo_{0.20}$-LDH/CC were depicted in Fig. S1 in the Electronic Supplementary Material (ESM). The initial step involved the reaction of $Co(NO_3)_2{\cdot}6H_2O$ with 2-methylimidazole (2-MIM) to form a solid ZIF-67 template on a conductive substrate (ZIF-67 on CC), resulting in an array of triangular nanosheets with a smooth surface. Subsequently, treatment of the ZIF-67/CC template with Na_2MoO_4 led to the formation of $CoMo_x$-LDH/CC via an ion exchange and etching process (Fig. S2 in the ESM), with a noticeable change in color from the uniform purple of the ZIF-67/CC film to the pale pink of the $CoMo_x$-LDH/CC catalysts. Field emission scanning electron microscopy (FESEM) analysis was then performed to investigate the microstructure of the synthesized samples, revealing the presence of evenly spread nanosheets for both ZIF-67/CC and $CoMo_x$-LDH/CC. Specifically, a smooth surface was observed for the ZIF-67/CC nanosheets (Fig. S3 in the ESM), which were transformed into wrinkle three-dimensional (3D) spatial nanosheets upon the doping of Mo to form $CoMo_x$-LDH/CC (Figs. 1(a)–1(j) and Figs. S4–S8 in the ESM). This transformation resulted in a porous 3D structure with interlacing curly nanosheets, providing more active sites for catalytic reactions and further accelerating mass transfer and gas release to improve the catalytic activity in the OER process. Furthermore, it was observed that the morphology of Co-LDH could be modified by varying the proportions of Mo etching. Figures 1(a) and 1(b), and Figs. S3 and S4 in the ESM revealed that $CoMo_{0.10}$-LDH/CC exhibited a slightly more wrinkle than the flattened ZIF-67/CC nanosheets, and this wrinkle increased gradually as the Mo content was raised to 0.15 g, as seen in Figs. 1(c) and 1(d), and Fig. S5 in the ESM. Comparing the FESEM diagram of $CoMo_{0.20}$-LDH/CC with ZIF-67/CC revealed that $CoMo_{0.20}$-LDH/CC had a uniform wrinkle distribution under stepwise magnification, leading to an increase in the area where the active sites could be distributed in comparison to ZIF-67/CC (Figs. 1(e) and 1(f), and Fig. S6 in the ESM). Conversely, the even higher Mo contents than 0.20 g resulted in the accumulation of more nanosheets, leading to a blocking in the cavity between the nanosheets (Figs. 1(g)–1(j) and Figs. S7 and S8 in the ESM). It finally affects the diffusion of electrolyte ions and the rapid release of oxygen bubbles, forming a physical barrier between the active site and the electrolyte. The energy dispersive spectrometer (EDS) mapping data demonstrated the uniform distribution of C, N, O, Co, and Mo on the $CoMo_{0.20}$-LDH/CC nanostructure, validating the successful incorporation of Mo ions into Co-LDH, consistent with the scanning electron microscopy (SEM) mapping results (Figs. S9 and S10 in the ESM). Transmission electron microscopy (TEM) images of the $CoMo_{0.20}$-LDH/CC nanosheets revealed a thin, almost translucent structure with symmetrical triangular tips and clear lattice fringes (Fig. 1(k)). Specifically, clear lattice fringes with a lattice spacing of 0.27 nm were assigned to the (100) plane of $CoMo_{0.20}$-LDH/CC (Figs. 1(l) and 1(m)). The selected area electron diffraction (SAED) (Fig. 1(n) and Fig. S12 in the ESM) also showed the crystal plane structure and crystallinity matching the high-resolution TEM (HRTEM) results. It was evident from Fig. S11 in the ESM that the as-synthesized ZIF-67/CC was an amorphous material, indicating that the electrode material shifted from amorphous to crystalline after the inclusion of the Mo source. The intermingling of amorphous and crystalline structures resulted in a plethora of kink sites between the ZIF-67/CC and $CoMo_{0.20}$-LDH/CC boundaries to promote adsorption. Figure 1(o) verified its layered structure as hydrotalcites [36]. Moreover, the EDS elemental mapping result (Figs. 1(p)–1(t)) and EDS line scanning and surface scanning results (Figs. 1(u) and 1(v)) clearly indicated the uniform distribution of Co, Mo, and O elements on the nanosheets, the region of surface scan was the area in Fig. 1(q), and the region of line scan was indicated by the arrow in Fig. 1(q), which clearly proved the successful synthesis of $CoMo_{0.20}$-LDH/CC.

Next, the crystal structures of $CoMo_x$-LDH/CC with varying Mo contents, ZIF-67/CC, and the CC substrate were analyzed using X-ray diffraction (XRD). The diffraction peaks in Fig. 2(a) clearly distinguish a typical $CoMo_x$-LDH/CC material ($CoMo_{0.20}$-LDH/CC) from ZIF-67/CC and CC. Figure 2(b) shows that these

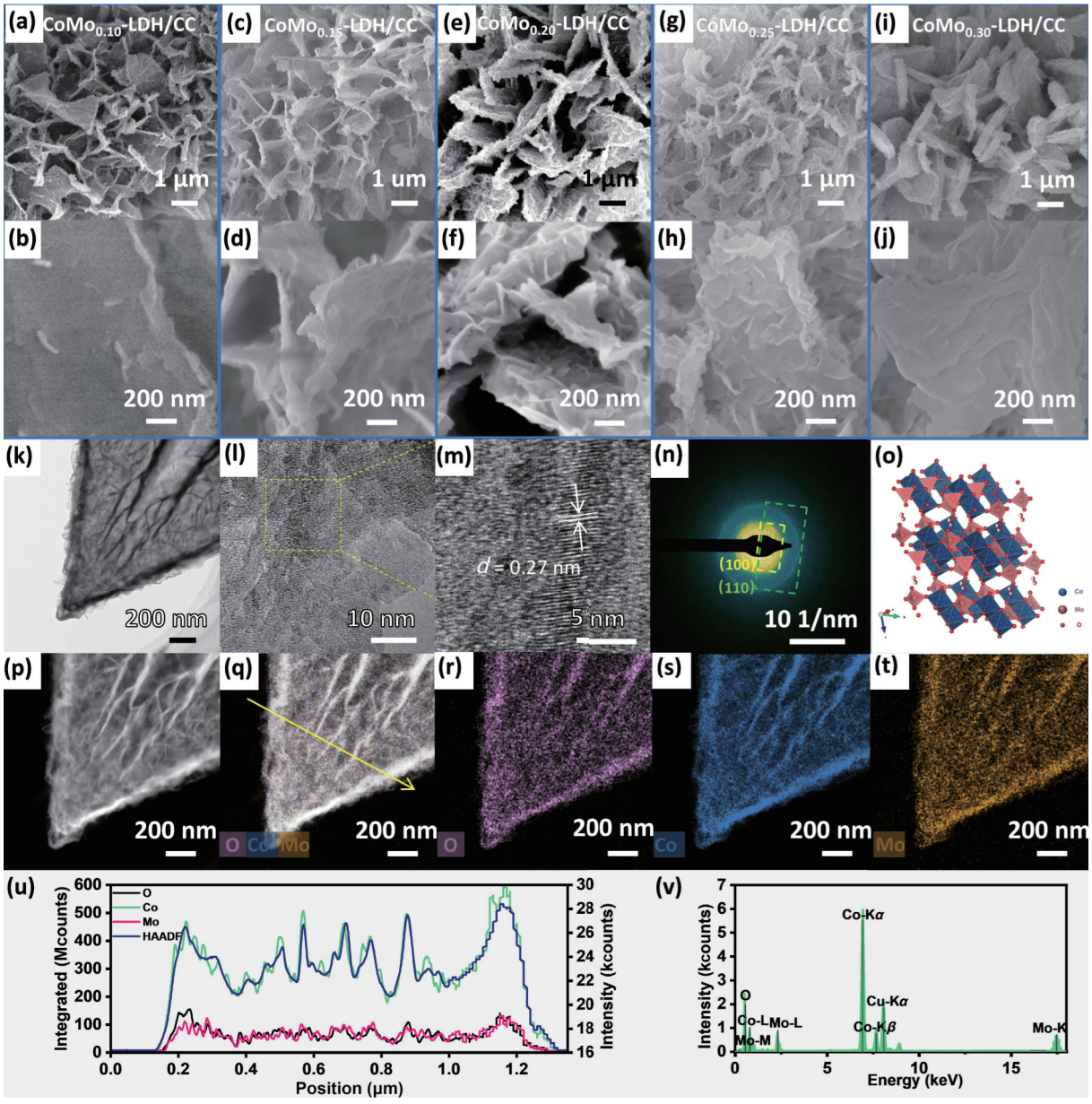

Figure 1 SEM images of (a) and (b) $CoMo_{0.10}$-LDH/CC; (c) and (d) $CoMo_{0.15}$-LDH/CC; (e) and (f) $CoMo_{0.20}$-LDH/CC; (g) and (h) $CoMo_{0.25}$-LDH/CC; (i) and (j) $CoMo_{0.30}$-LDH/CC. (k) TEM images of $CoMo_{0.20}$-LDH/CC; (l) and (m) HRTEM image of $CoMo_{0.20}$-LDH/CC; (n) SAED pattern of $CoMo_{0.20}$-LDH/CC; (o) polyhedral representations of the structures of $CoMo_{0.20}$-LDH/CC; (p)–(t) HAADF-TEM image and EDS mapping of O, Co, and Mo of $CoMo_{0.20}$-LDH/CC; (u) EDS line scan area is the area through which the yellow line in (q) passes; (v) EDS image of in the area of (q).

$CoMo_x$-LDH/CC materials displayed similar XRD patterns with the representative diffraction peaks at 11.8°, 23.5°, 33.5°, and 59.8°, corresponding to the (003), (006), (100), and (110) planes of $CoMo_x$-LDH/CC, respectively (JCPDS No. 46-0605). Additionally, X-ray photoelectron spectroscopy (XPS) was used to investigate the composition and chemical states of ZIF-67/CC and $CoMo_x$-LDH/CC. The XPS survey spectrum of ZIF-67/CC (Fig. S14 in the ESM) was categorized into C, N, O and Co groups, which was in line with the EDS mapping results. Furthermore, Figs. S14(b)–S14(e) in the ESM displayed high-resolution XPS spectra for the Co 2p, O 1s, C 1s and N 1s signals, respectively, confirming the successful formation of ZIF-67 on the CC [37–39]. On the other hand, the XPS survey spectra of $CoMo_x$-LDH/CC in Figs. 2(c)–2(e) indicated the presence of Co, Mo and O as primary elements. The high-resolution Co 2p spectra were divided into two regions, namely the Co $2p_{1/2}$ and Co $2p_{3/2}$ regions (Fig. 2(c)). In the Co $2p_{3/2}$ region, three characteristic peaks centered at 782.5, 780.5, and 786.8 eV were assigned as Co^{2+}, Co^{3+}, and the satellite peak, respectively, and their corresponding Co $2p_{1/2}$ peaks were positioned at 798.2, 798.2, and 802.3 eV. These results suggested the co-existence of both Co^{2+} and Co^{3+} in the $CoMo_x$-LDH/CC [40–42]. The Mo 3d XPS spectrum of these materials, as illustrated in Fig. 2(d), revealed the representative peaks of Mo $3d_{5/2}$ and Mo $3d_{3/2}$ at binding energies with 232.2 and 235.6 eV, respectively, consistent with hexavalent Mo in MoO_3 [43]. As the weight of the Mo source further increased to 0.20 g, a notable 0.4 eV shift towards higher binding energies was observed in the Co^{2+} peaks. It is shown that the chemical environment of Co in $CoMo_x$-LDH/CC materials has changed, and its transition to high binding energy indicates that the bivalent Co is in high oxidation state. This may be attributed to the electron transfer from Co to Mo via the bridging oxygen in $CoMo_x$-LDH/CC materials [26]. Moreover, because the positive shift of binding energy is related to the expansion of the bond, the bonding strength between the Co site and the O-containing intermediate is weakened, and Co is promoted as the active site to further release O_2. Then, as the mass of Mo increases, the content of Co^{3+} can be seen to increase. It is worth noting that from $CoMo_{0.20}$-LDH/CC to $CoMo_{0.25}$-LDH/CC,

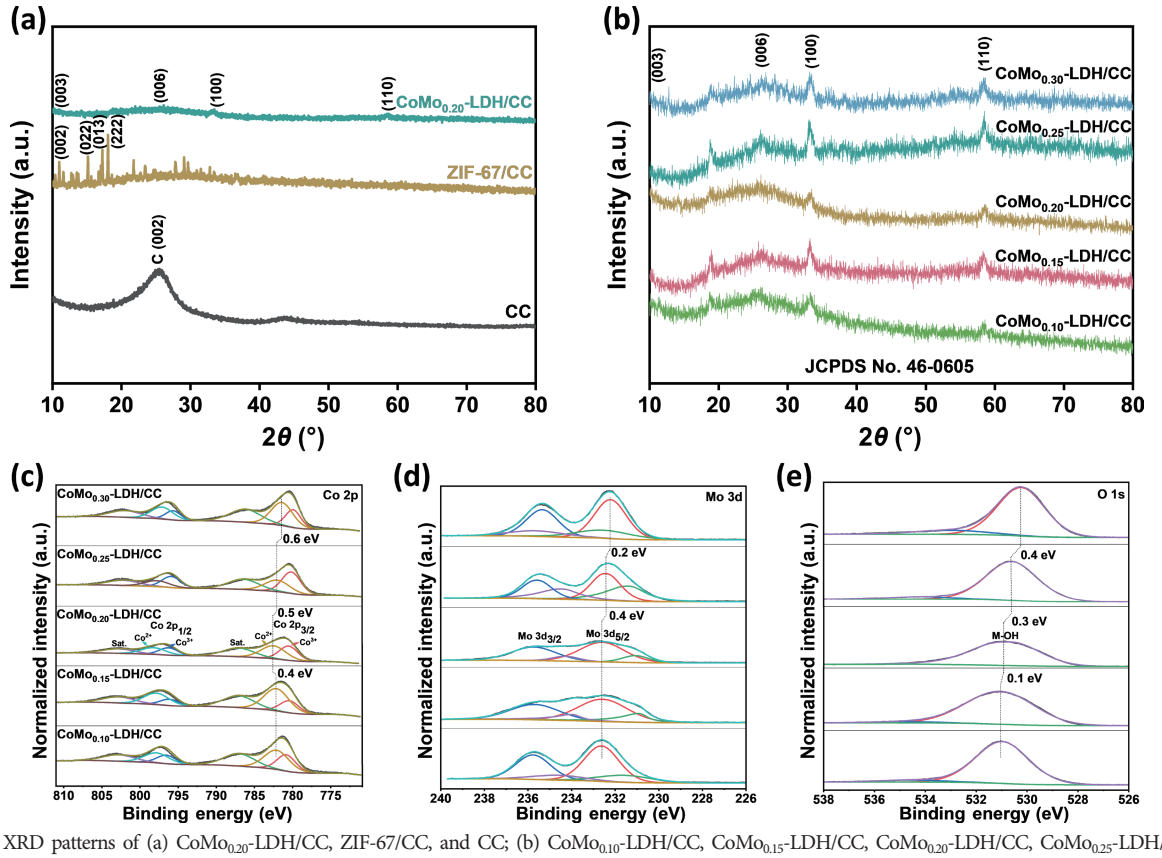

Figure 2 XRD patterns of (a) $CoMo_{0.20}$-LDH/CC, ZIF-67/CC, and CC; (b) $CoMo_{0.10}$-LDH/CC, $CoMo_{0.15}$-LDH/CC, $CoMo_{0.20}$-LDH/CC, $CoMo_{0.25}$-LDH/CC, and $CoMo_{0.30}$-LDH/CC. High-resolution XPS spectra of $CoMo_x$-LDH/CC: (c) Co 2p, (d) Mo 3d, and (e) O 1s.

and finally to $CoMo_{0.30}$-LDH/CC, the peak value of O 1s moves in the direction of small binding. Figure 2(e) displayed the O 1s spectrum of these array-type catalysts. The main characteristic peak is M–OH and the binding energy range is 530.8 eV. This is clearly characteristic of oxygen binding to species with higher valence states, in this case mainly Co^{3+} or Mo^{6+} compounds. To further understand the surface properties of $CoMo_x$-LDH/CC, contact angle measurements were conducted using a contact angle meter (Fig. S13 in the ESM). The hydrophilicity of CC after acid treatment was evident, as indicated by a contact angle of 135° for the ZIF-67/CC electrode and 0° for the $CoMo_x$-LDH/CC electrode, demonstrating the improved hydrophilicity and thereby enhancing its activity and durability.

We sought to evaluate the electrochemical OER performance of the $CoMo_x$-LDH/CC catalysts and ZIF-67/CC arrays in a 1 M KOH electrolyte using a standard three-electrode system. As illustrated in Fig. 3(a), the bare CC could not reach the current density of 50 $mA{\cdot}cm^{-2}$ in the tested voltage range, suggesting that the substrate had negligible OER performance.

Subsequently, the precursor material (ZIF-67/CC) displayed moderate OER traits, whereas the target materials ($CoMo_x$-LDH/CC) exhibited considerably improved OER performance, demonstrating the significant effect of the Mo source on the promotion of the OER process. Notably, $CoMo_{0.20}$-LDH/CC exhibited the highest activity in the OER, as evidenced by the minimum overpotential of 288 mV at a current density of 50 $mA{\cdot}cm^{-2}$. By contrast, $CoMo_{0.10}$-LDH/CC, $CoMo_{0.15}$-LDH/CC, $CoMo_{0.25}$-LDH/CC, $CoMo_{0.30}$-LDH/CC, and ZIF-67/CC exhibited overpotential of 319, 311, 297, 322, and 330 mV, respectively, at the same current density of 50 $mA{\cdot}cm^{-2}$. When the current density was increased to 100 $mA{\cdot}cm^{-2}$, $CoMo_{0.20}$-LDH/CC still manifested the lowest overpotential of 306 mV among all the samples (Fig. 3(b)). These results underscored the high catalytic performance of $CoMo_{0.20}$-LDH/CC in the OER under alkaline conditions.

Moreover, $CoMo_{0.20}$-LDH/CC demonstrated the smallest Tafel slope of 60 $mV{\cdot}dec^{-1}$ among all the investigated catalysts, highlighting its excellent OER kinetics (as shown in Fig. 3(c)). Additionally, the double-layer capacitance (C_{dl}) value of $CoMo_{0.20}$-LDH/CC was greater than those of the other catalysts (Figs. S15 and S16(a) in the ESM), registering at 23.2 $mF{\cdot}cm^{-2}$. Due to the positive correlation between electrochemical surface area (ECSA) and C_{dl}, $CoMo_{0.20}$-LDH/CC still demonstrated the highest inherent activity in terms of normalizing the electrochemical activity via ECSA [44, 45]. In comparison with the other $CoMo_x$-LDH/CC samples, ZIF-67/CC has the smallest electrochemically active surface area, which may be related to its flat nanosheets. According to ECSA-normalized LSV curves (Fig. 3(d)), under a current density of 0.30 $mA{\cdot}cm^{-2}$, $CoMo_{0.20}$-LDH/CC still displayed the lowest overpotential compared to the other samples, cementing its highest intrinsic catalytic capability. The ranking of the $CoMo_x$-LDH/CC arrays with varying Mo content remained constant, with $CoMo_{0.20}$-LDH/CC exhibiting the lowest overpotential at 308 mV, followed by $CoMo_{0.25}$-LDH/CC at 320 mV, $CoMo_{0.15}$-LDH/CC at 331 mV, CoMo0.10-LDH/CC at 346 mV, and $CoMo_{0.30}$-LDH/CC at 359 mV. Additionally, the comparison of the OER performance between $CoMo_{0.20}$-LDH/CC and a variety of reported LDH-based catalysts was made at a current density of 10 $mA{\cdot}cm^{-2}$ (as depicted in Fig. 3(e) and Table S1 in the ESM for details). It was worth emphasizing that our best-performing $CoMo_{0.20}$-LDH/CC catalyst not only featured a straightforward production process, but also held great potential in terms of electrochemical activity.

Furthermore, electrochemical impedance spectroscopy (EIS) results demonstrated that $CoMo_{0.20}$-LDH/CC had the lowest charge transfer resistance, thus resulting in the quickest electron transfer rate (Fig. 3(f)), which further indicated that $CoMo_{0.20}$-LDH/CC was the most effective material in terms of intrinsic catalytic activity for OER. Based on the electrochemical tests mentioned above, it is evident that $CoMo_x$-LDH/CC exhibits superior performance when the Mo content is 0.20 g. This improvement in performance is attributed to the changes in

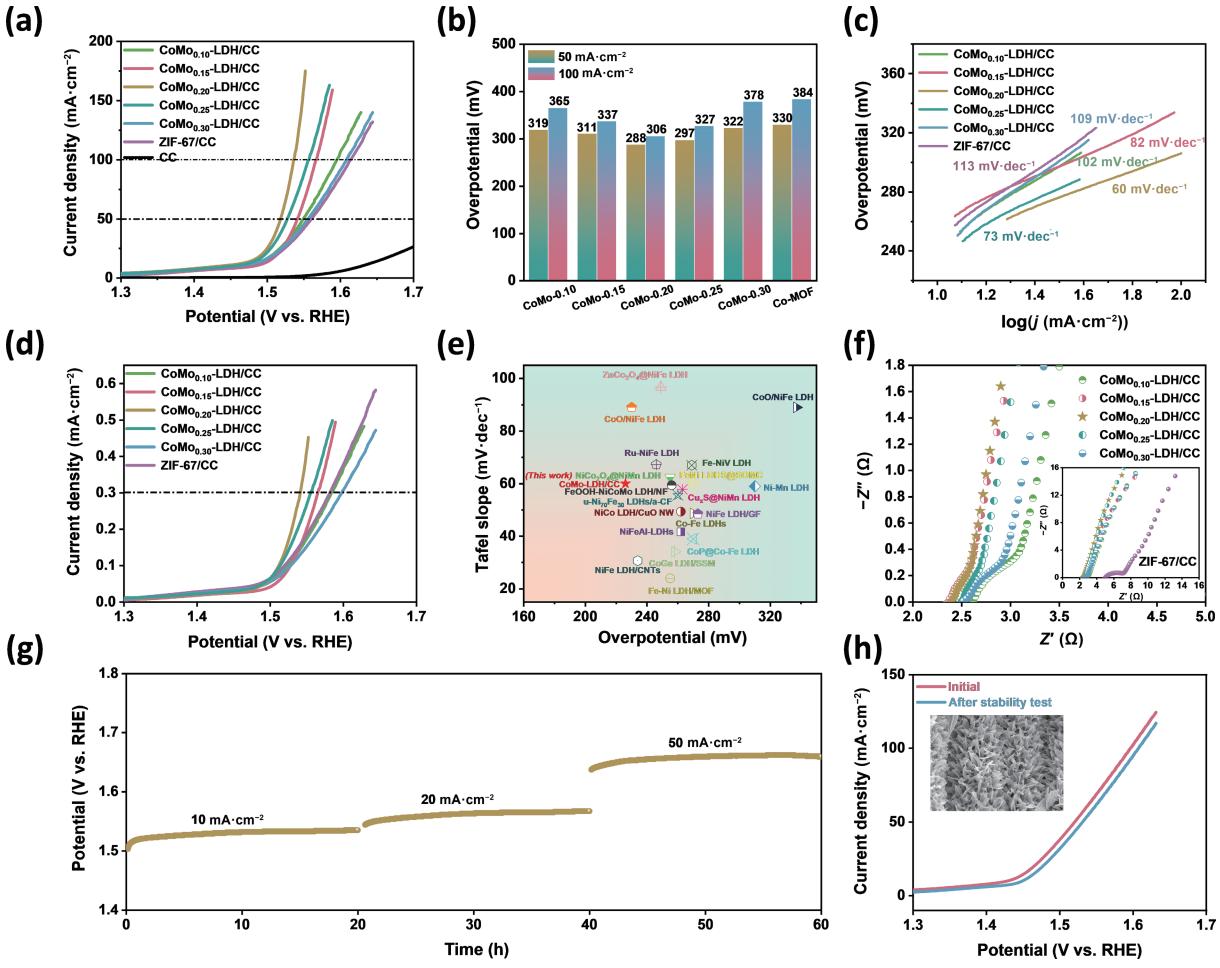

Figure 3 (a) OER polarization curves; (b) histogram of the corresponding overpotential values of different samples at current densities of 50 mA cm^{-2} and 100 mA cm^{-2}, respectively; (c) Tafel slopes; (d) OER polarization curves after normalizing the electrochemical activity via ECSA; (e) reported properties of OER non-noble metal LDH electrocatalysts in alkaline electrolytes; (f) EIS test; (g) chronoamperometry measurements at three different current densities of 10, 20, and 50 mA·cm^{-2}; (h) OER polarization curves of before and after stability test.

morphology, specifically the presence of more wrinkles and less accumulation on the array at this Mo content. Consequently, this allows for increased ion flow and a larger surface area, providing more active sites.

Furthermore, the stability of the best-performing catalyst ($CoMo_{0.20}$-LDH/CC) was assessed since this parameter is critical for the suitability of a catalyst in industrial applications. Throughout a 60-hour period, we subjected $CoMo_{0.20}$-LDH/CC to three different current densities of 10, 20, and 50 mA·cm^{-2}, respectively, maintaining a constant current. The results, as depicted in Fig. 3(g), revealed an insignificant increase in voltage, suggesting the good long-term durability of this catalyst. Subsequently, a comparison of the $CoMo_{0.20}$-LDH/CC sample before and after the stability test (Fig. 3(h)) indicated minimal change in overpotential at the same current density, further confirming the sample's stability. Moreover, the inset in the figures demonstrated little variation in the electrode surface morphology following the electrochemical reaction. The stability of ZIF-67/CC was also tested and shown in Fig. S16(b) in the ESM.

Further electrochemical device investigations were carried out to assess capability of $CoMo_{0.20}$-LDH/CC in promoting the overall water decomposition. Accordingly, a two-electrode system consisting of the optimized $CoMo_{0.20}$-LDH/CC as the anode and Pt/C on CC as the cathode, denoted as $CoMo_{0.20}$-LDH/CC (+)//Pt/C@CC(−), was implemented (Fig. 4(a)) [46]. For comparison, a similar system utilizing Ir/C on CC as the anode and Pt/C on CC as the cathode, represented as Ir/C@CC(+)//Pt/C@CC(−), was also assembled. At a current density of 10 mA·cm^{-2}, the $CoMo_{0.20}$-LDH/CC (+)//Pt/C@CC(−) device has a battery potential of 1.611 V (Fig. 4(b)), which is lower than that of the Ir/C@CC(+)//Pt/C@CC(−) system (1.651 V), suggesting the promising application potential of the newly developed system in this study. Furthermore, our two-electrode system demonstrates prolonged stability at the current density of 10 mA·cm^{-2}, as evidenced by the minimal voltage fluctuation over a 20 h timeframe (Fig. 4(c)). These results indicate that the synthesized $CoMo_{0.20}$-LDH/CC catalyst holds promise as a substitute for precious metal catalysts in water electrolysis.

3 Conclusions

In summary, a series of $CoMo_x$-LDH/CC arrays were developed via a simple and facile synthetic strategy. The approach involved creating ZIF-67/CC arrays by cultivating ZIF-67 onto CC substrates, and then introducing a Mo source with varying weight loadings to produce the $CoMo_x$-LDH/CC arrays as the desired materials. It is worth noting that the direct growth of $CoMo_x$-LDH nanosheets on CC negates the need for adhesives, thereby leading to reduced contact resistance and increased superhydrophilicity. Additionally, comprehensive characterizations of the materials indicated that the shift in morphology and the accumulation of nanosheets have an impact on the exposure of catalyst active sites and the transfer of ions in the electrolyte. Moreover, the catalytic performance of the as-prepared arrays in the OER was systematically explored. It was found that the precursor material ZIF-67/CC exhibited moderate electrochemical activity and longevity. By contrast, the introduction of Mo significantly altered

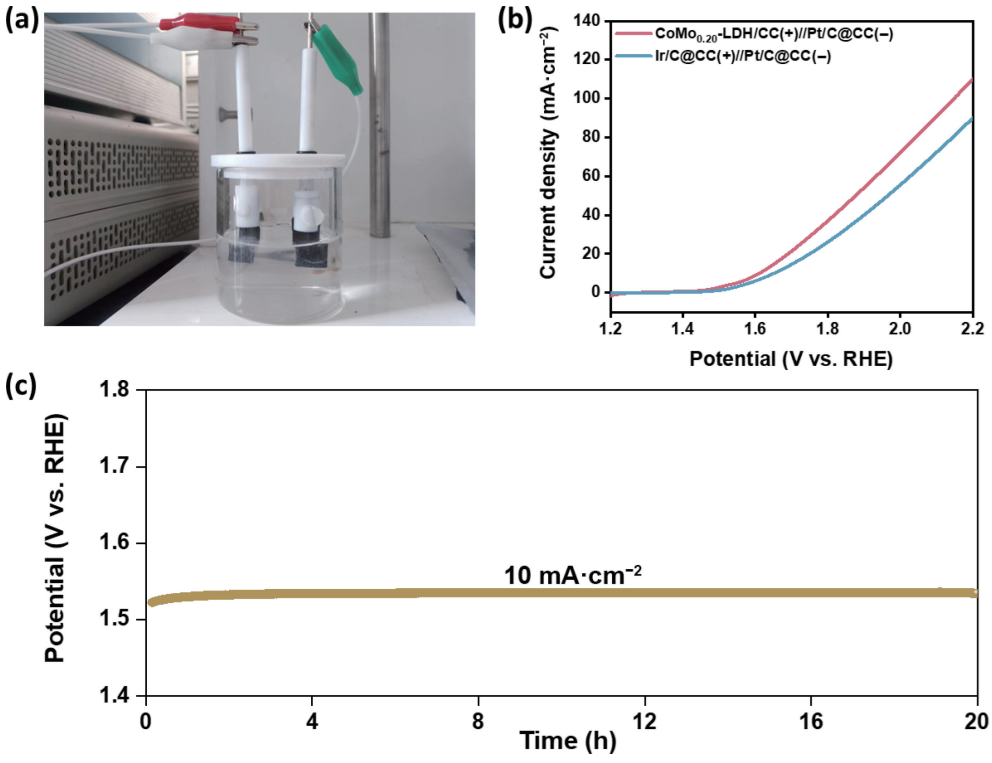

Figure 4 (a) The digital photograph of the two-electrode system; (b) polarization curves of $CoMo_{0.20}$-LDH/CC (+)//Pt/C@CC(–) and Ir/C@CC(+)//Pt/C@CC(–) for overall water splitting; (c) long-term stability test of $CoMo_{0.20}$-LDH/CC (+)//Pt/C@CC(–) for overall water splitting.

the crystal lattice of the original ZIF-67/CC, thereby enhancing the activity and durability of the resulting $CoMo_x$-LDH/CC catalysts. Specifically, the $CoMo_{0.20}$-LDH/CC catalyst exhibits optimal catalytic activity, as evidenced by the lowest overpotential of 226 mV at 10 mA·cm^{-2} and the maximum C_{dl} value of 23.2 mF·cm^{-2}, highlighting the importance of a rational bimetallic molar ratio in attaining remarkable OER activity. This research presents new opportunities for designing low-cost, practical, and high-performance OER catalysts for energy storage.

Acknowledgements

This work acknowledges the financial support of the Fundamental Research Funds for the Central Universities (No. 40120631) and the National Natural Science Foundation of China (No. 52202291) for the support. C. C. acknowledges the financial support of Natural Science Foundation of Hubei Province (No. 2022CFB388) and the Natural Science Foundation of Hainan Province of China (No. 623MS068).

Electronic Supplementary Material: Supplementary material (Experimental section, the sample digital images, supplementary characterization spectra (Figs. S1–S16), and a comparison table (Table S1)) is available in the online version of this article at https://doi.org/10.1007/s12274-024-6529-1.

References

[1] Turner, J. A. Sustainable hydrogen production. *Science* **2004**, *305*, 972–974.

[2] Jamesh, M. I. Recent progress on earth abundant hydrogen evolution reaction and oxygen evolution reaction bifunctional electrocatalyst for overall water splitting in alkaline media. *J. Power Sources* **2016**, *333*, 213–236.

[3] Jamesh, M. I.; Sun, X. M. Recent progress on earth abundant electrocatalysts for oxygen evolution reaction (OER) in alkaline medium to achieve efficient water splitting—A review. *J. Power Sources* **2018**, *400*, 31–68.

[4] Chen, Z. L.; Qing, H. L.; Zhou, K.; Sun, D. L.; Wu, R. B. Metal-organic framework-derived nanocomposites for electrocatalytic hydrogen evolution reaction. *Prog. Mater. Sci.* **2020**, *108*, 100618.

[5] Armaroli, N.; Balzani, V. Solar electricity and solar fuels: Status and perspectives in the context of the energy transition. *Chem. —Eur. J.* **2016**, *22*, 32–57.

[6] Chu, S.; Majumdar, A. Opportunities and challenges for a sustainable energy future. *Nature* **2012**, *488*, 294–303.

[7] Faber, M. S.; Jin, S. Earth-abundant inorganic electrocatalysts and their nanostructures for energy conversion applications. *Energy Environ. Sci.* **2014**, *7*, 3519–3542.

[8] Zhang, K. X.; Zou, R. Q. Advanced transition metal-based OER electrocatalysts: Current status, opportunities, and challenges. *Small* **2021**, *17*, 2100129.

[9] Reddy, M. S. B.; Aich, S. Recent progress in surface and heterointerface engineering of 2D MXenes for gas sensing applications. *Coord. Chem. Rev.* **2024**, *500*, 215542.

[10] Wang, W.; Liu, Y. C.; Li, J.; Luo, J.; Fu, L.; Chen, S. L. NiFe LDH nanodots anchored on 3D macro/mesoporous carbon as a high-performance ORR/OER bifunctional electrocatalyst. *J. Mater. Chem. A* **2018**, *6*, 14299–14306.

[11] Xiao, G. L.; Chen, W. B.; Cai, Y. M.; Zhang, S. F.; Wang, D.; Cai, D. D. Facile synthesis of sulfate-intercalated CoFe LDH nanosheets derived from two-dimensional ZIF-9(III) for promoted oxygen evolution reaction. *Catalysts* **2022**, *12*, 688.

[12] Yan, X. S.; Wang, Z. L.; Bao, J.; Song, Y. H.; She, X. J.; Yuan, J. J.; Hua, Y. J.; Lv, G. A.; Li, H. M.; Xu, H. CoMo layered double hydroxide equipped with carbon nanotubes for electrocatalytic oxygen evolution reaction. *Nanotechnology* **2023**, *34*, 065401.

[13] Ye, C.; Zhang, L. C.; Yue, L. C.; Deng, B.; Cao, Y.; Liu, Q.; Luo, Y. L.; Lu, S. Y.; Zheng, B. Z.; Sun, X. P. A NiCo LDH nanosheet array on graphite felt: An efficient 3D electrocatalyst for the oxygen evolution reaction in alkaline media. *Inorg. Chem. Front.* **2021**, *8*, 3162–3166.

[14] Zhang, M. L.; Wang, J. L.; Ma, L. F.; Gong, Y. Q. Spontaneous synthesis of silver nanoparticles on cobalt-molybdenum layer double hydroxide nanocages for improved oxygen evolution reaction. *J. Colloid Interface Sci.* **2022**, *628*, 299–307.

[15] Zhang, B.; Wang, L.; Cao, Z.; Kozlov, S. M.; García de Arquer, F. P.; Dinh, C. T.; Li, J.; Wang, Z. Y.; Zheng, X. L.; Zhang, L. S. et al. High-valence metals improve oxygen evolution reaction performance by modulating 3d metal oxidation cycle energetics. *Nat.*

Catal. **2020**, *3*, 985–992.
[16] Dai, R. R.; Dai, C. Y.; Hou, S. J.; He, Q. J.; Liu, B. G.; Huang, M. H.; Jiang, H. Q.; Li, M. H.; Pan, L. K.; Guo, Z. et al. Opportunities and challenges of hydrotalcite-related electrocatalysts for seawater splitting: A systematic perspective from materials synthesis, characterization and application. *J. Mater. Chem. A* **2023**, *11*, 20383–20407.
[17] Gebreslase, G. A.; Martínez-Huerta, M. V.; Lázaro, M. J. Recent progress on bimetallic NiCo and CoFe based electrocatalysts for alkaline oxygen evolution reaction: A review. *J. Energy Chem.* **2022**, *67*, 101–137.
[18] Hameed, A.; Batool, M.; Liu, Z. Y.; Nadeem, M. A.; Jin, R. C. Layered double hydroxide-derived nanomaterials for efficient electrocatalytic water splitting: Recent progress and future perspective. *ACS Energy Lett.* **2022**, *7*, 3311–3328.
[19] Kulkarni, R.; Lingamdinne, L. P.; Karri, R. R.; Momin, Z. H.; Koduru, J. R.; Chang, Y. Y. Catalytic efficiency of LDH@carbonaceous hybrid nanocomposites towards water splitting mechanism: Impact of plasma and its significance on HER and OER activity. *Coord. Chem. Rev.* **2023**, *497*, 215460.
[20] Sahoo, D. P.; Das, K. K.; Mansingh, S.; Sultana, S.; Parida, K. Recent progress in first row transition metal layered double hydroxide (LDH) based electrocatalysts towards water splitting: A review with insights on synthesis. *Coord. Chem. Rev.* **2022**, *469*, 214666.
[21] Zhang, L.; Zhu, J. W.; Li, X.; Mu, S. C.; Verpoort, F.; Xue, J. M.; Kou, Z. K.; Wang, J. Nurturing the marriages of single atoms with atomic clusters and nanoparticles for better heterogeneous electrocatalysis. *Interdiscip. Mater.* **2022**, *1*, 51–87.
[22] Zhou, D. J.; Li, P. S.; Lin, X.; McKinley, A.; Kuang, Y.; Liu, W.; Lin, W. F.; Sun, X. M.; Duan, X. Layered double hydroxide-based electrocatalysts for the oxygen evolution reaction: Identification and tailoring of active sites, and superaerophobic nanoarray electrode assembly. *Chem. Soc. Rev.* **2021**, *50*, 8790–8817.
[23] Yu, J.; Yu, F.; Yuen, M. F.; Wang, C. D. Two-dimensional layered double hydroxides as a platform for electrocatalytic oxygen evolution. *J. Mater. Chem. A* **2021**, *9*, 9389–9430.
[24] Hu, J.; Tang, X. M.; Dai, Q.; Liu, Z. Q.; Zhang, H. M.; Zheng, A. M.; Yuan, Z. Z.; Li, X. F. Layered double hydroxide membrane with high hydroxide conductivity and ion selectivity for energy storage device. *Nat. Commun.* **2021**, *12*, 3409.
[25] Mehdi, M.; An, B. S.; Kim, H.; Lee, S.; Lee, C.; Seo, M.; Noh, M. W.; Cho, W. C.; Kim, C. H.; Choi, C. H. et al. Rational design of a stable Fe-rich Ni-Fe layered double hydroxide for the industrially relevant dynamic operation of alkaline water electrolyzers. *Adv. Energy Mater.* **2023**, *13*, 2204403.
[26] Kou, Z. K.; Yu, Y.; Liu, X. M.; Gao, X. R.; Zheng, L. R.; Zou, H. Y.; Pang, Y. J.; Wang, Z. Y.; Pan, Z. H.; He, J. Q. et al. Potential-dependent phase transition and Mo-enriched surface reconstruction of γ-CoOOH in a heterostructured Co-Mo_2C precatalyst enable water oxidation. *ACS Catal.* **2020**, *10*, 4411–4419.
[27] Liu, B. R.; Zhang, N.; Ma, M. M. Cobalt-based nanosheet arrays as efficient electrocatalysts for overall water splitting. *J. Mater. Chem. A* **2017**, *5*, 17640–17646.
[28] Mishra, I. K.; Zhou, H. Q.; Sun, J. Y.; Qin, F.; Dahal, K.; Bao, J. M.; Chen, S.; Ren, Z. F. Hierarchical CoP/Ni_5P_4/CoP microsheet arrays as a robust pH-universal electrocatalyst for efficient hydrogen generation. *Energy Environ. Sci.* **2018**, *11*, 2246–2252.
[29] Wang, C. H.; Li, Y. H.; Gu, C. D.; Zhang, L. J.; Wang, X. L.; Tu, J. P. Active Co@CoO core/shell nanowire arrays as efficient electrocatalysts for hydrogen evolution reaction. *Chem. Eng. J.* **2022**, *429*, 132226.
[30] Mishra, I. K.; Zhou, H. Q.; Sun, J. Y.; Dahal, K.; Ren, Z. S.; He, R.; Chen, S.; Ren, Z. F. Highly efficient hydrogen evolution by self-standing nickel phosphide-based hybrid nanosheet arrays electrocatalyst. *Mater. Today Phys.* **2018**, *4*, 1–6.
[31] Cheng, W. R.; Zhang, H.; Zhao, X.; Su, H.; Tang, F. M.; Tian, J.; Liu, Q. H. A metal-vacancy-solid-solution NiAlP nanowall array bifunctional electrocatalyst for exceptional all-pH overall water splitting. *J. Mater. Chem. A* **2018**, *6*, 9420–9427.
[32] Hao, S.; Yang, Y. C. Water splitting in near-neutral media: Using an Mn-Co-based nanowire array as a complementary electrocatalyst. *J. Mater. Chem. A* **2017**, *5*, 12091–12095.
[33] Luo, J. S.; Im, J. H.; Mayer, M. T.; Schreier, M.; Nazeeruddin, M. K.; Park, N. G.; Tilley, S. D.; Fan, H. J.; Grätzel, M. Water photolysis at 12.3% efficiency via perovskite photovoltaics and Earth-abundant catalysts. *Science* **2014**, *345*, 1593–1596.
[34] Wang, Y. J.; Cao, Q. H.; Guan, C.; Cheng, C. W. Recent advances on self-supported arrayed bifunctional oxygen electrocatalysts for flexible solid-state Zn-air batteries. *Small* **2020**, *16*, 2002902.
[35] Wang, Y.; Sun, Y.; Yan, F.; Zhu, C. L.; Gao, P.; Zhang, X. T.; Chen, Y. J. Self-supported NiMo-based nanowire arrays as bifunctional electrocatalysts for full water splitting. *J. Mater. Chem. A* **2018**, *6*, 8479–8487.
[36] Eda, K.; Uno, Y.; Nagai, N.; Sotani, N.; Whittingham, M. S. Crystal structure of cobalt molybdate hydrate $CoMoO_4 \cdot nH_2O$. *J. Solid State Chem.* **2005**, *178*, 2791–2797.
[37] Li, X.; Li, Z. H.; Lu, L.; Huang, L. M.; Xiang, L.; Shen, J.; Liu, S. Y.; Xiao, D. R. The solvent induced inter-dimensional phase transformations of cobalt zeolitic-imidazolate frameworks. *Chem.—Eur. J.* **2017**, *23*, 10638–10643.
[38] Xu, F. G.; Wang, L. W.; Wu, M. J.; Ma, G. R. Vertical growth of leaf-like Co-metal organic framework on carbon fiber cloth as integrated electrode for sensitive detection of dopamine and uric acid. *Sens. Actuators B Chem.* **2023**, *386*, 133734.
[39] Zhang, J. C.; Zhang, T. C.; Yu, D. B.; Xiao, K. S.; Hong, Y. Transition from ZIF-L-Co to ZIF-67: A new insight into the structural evolution of zeolitic imidazolate frameworks (ZIFs) in aqueous systems. *CrystEngComm* **2015**, *17*, 8212–8215.
[40] Chen, T.; Li, S. Z.; Wen, J.; Gui, P. B.; Guo, Y. X.; Guan, C.; Liu, J. P.; Fang, G. J. Rational construction of hollow core-branch $CoSe_2$ nanoarrays for high-performance asymmetric supercapacitor and efficient oxygen evolution. *Small* **2018**, *14*, 1700979.
[41] Fang, L.; Li, W. X.; Guan, Y. X.; Feng, Y. Y.; Zhang, H. J.; Wang, S. L.; Wang, Y. Tuning unique peapod-like $Co(S_xSe_{1-x})_2$ nanoparticles for efficient overall water splitting. *Adv. Funct. Mater.* **2017**, *27*, 1701008.
[42] Lin, J. H.; Wang, H. H.; Yan, Y. T.; Zheng, X. H.; Jia, H. N.; Qi, J. L.; Cao, J.; Tu, J. C.; Fei, W. D.; Feng, J. C. Core-branched $CoSe_2$/$Ni_{0.85}Se$ nanotube arrays on Ni foam with remarkable electrochemical performance for hybrid supercapacitors. *J. Mater. Chem. A* **2018**, *6*, 19151–19158.
[43] Wang, X. Q.; Zheng, B. J.; Yu, B.; Wang, B.; Hou, W. Q.; Zhang, W. L.; Chen, Y. F. *In situ* synthesis of hierarchical $MoSe_2$-$CoSe_2$ nanotubes as an efficient electrocatalyst for the hydrogen evolution reaction in both acidic and alkaline media. *J. Mater. Chem. A* **2018**, *6*, 7842–7850.
[44] Mele, A.; Dickinson, P.; Mattei, M. A holistic physics-based observer for online flooding and ECSA loss detection in FCEV. *Int. J. Hydrog. Energy* **2024**, *55*, 1393–1404.
[45] Paul, R.; Zhai, Q. F.; Roy, A. K.; Dai, L. M. Charge transfer of carbon nanomaterials for efficient metal-free electrocatalysis. *Interdiscip. Mater.* **2022**, *1*, 28–50.
[46] Jiang, J.; Liu, J. P. Iron anode-based aqueous electrochemical energy storage devices: Recent advances and future perspectives. *Interdiscip. Mater.* **2022**, *1*, 116–139.